

Beam distortion due to gold fiducial markers during salvage high-intensity focused ultrasound in the prostate

P. S. Georgiou^{a)}

Department of Medical Physics and Biomedical Engineering, University College London, London, UK

J. Jaros

Faculty of Information Technology, Brno University of Technology, Brno, Czech Republic

H. Payne

Department of Medical Physics and Biomedical Engineering, University College London, London, UK

Department of Oncology, University College London Hospitals, London, UK

C. Allen

Department of Oncology, University College London Hospitals, London, UK

T. T. Shah and H. U. Ahmed

Division of Surgery and Interventional Science, University College London, London, UK

E. Gibson, D. Barratt, and B. E. Treeby

Department of Medical Physics and Biomedical Engineering, University College London, London, UK

(Received 23 August 2016; revised 21 October 2016; accepted for publication 17 November 2016; published 13 February 2017)

Purpose: High intensity focused ultrasound (HIFU) provides a non-invasive salvage treatment option for patients with recurrence after external beam radiation therapy (EBRT). As part of EBRT the prostate is frequently implanted with permanent fiducial markers. To date, the impact of these markers on subsequent HIFU treatment is unknown. The objective of this work was to systematically investigate, using computational simulations, how these fiducial markers affect the delivery of HIFU treatment.

Methods: A series of simulations was performed modelling the propagation of ultrasound pressure waves in the prostate with a single spherical or cylindrical gold marker at different positions and orientations. For each marker configuration, a set of metrics (spatial-peak temporal-average intensity, focus shift, focal volume) was evaluated to quantify the distortion introduced at the focus. An analytical model was also developed describing the marker effect on the intensity at the focus. The model was used to examine the marker's impact in a clinical setting through case studies.

Results: The simulations show that the presence of the marker in the pre-focal region causes reflections which induce a decrease in the focal intensity and focal volume, and a shift of the maximum pressure point away from the transducer's focus. These effects depend on the shape and orientation of the marker and become more pronounced as its distance from the transducer's focus decreases, with the distortion introduced by the marker greatly increasing when placed within 5 mm of the focus. The analytical model approximates the marker's effect and can be used as an alternative method to the computationally intensive and time consuming simulations for quickly estimating the intensity at the focus. A retrospective review of a small patient cohort selected for focal HIFU after failed EBRT indicates that the presence of the marker may affect HIFU treatment delivery.

Conclusions: The distortion introduced by the marker to the HIFU beam when positioned close to the focus may result in an undertreated region beyond the marker due to less energy arriving at the focus, and an overtreated region due to reflections. Further work is necessary to investigate whether the results presented here justify the revision of the patient selection criteria or the markers' placement protocol. © 2016 American Association of Physicists in Medicine [<https://doi.org/10.1002/mp.12044>]

Key words: EBRT, fiducial marker, prostate cancer, salvage HIFU

1. INTRODUCTION

Prostate cancer is the most commonly occurring male cancer and the second leading cause of cancer-related death in men in the European Union (EU) and the United States of

America (USA).^{1,2} More specifically, in 2012 of all reported cancer cases in men, prostate cancer accounted for 24.1% in the EU, with a 10% mortality rate, and 28.3% in the USA, with a 9.4% mortality.¹ According to the American Cancer Society, these rates are estimated to continue in 2016.³ These

figures differ when viewed based on worldwide data, where prostate cancer appears as the second most diagnosed cancer in men with 1.1 million diagnosed cases in 2012 (14.8%) and as the fifth cause of cancer-related death with 307 thousand deaths (6.6%).^{1,4} Despite the lower incidence and mortality rates from worldwide data, prostate cancer is still one of the major malignancies affecting hundreds of thousands of men each year and improving its diagnosis and treatment is of great importance.

There is a range of available options for treating prostate cancer with some of them having a curative intent and others palliative. Selecting an appropriate therapy depends on several factors, such as the stage of the tumor, biochemical indicators (e.g. prostate specific antigen value), Gleason score, other associated diseases, the patient's age and life expectancy, as well as the patient's personal preference.⁵ For localized or locally advanced prostate cancer, recommended treatments for primary therapy include active surveillance, radical prostatectomy (RP), external beam radiation therapy (EBRT) and temporary (high-dose rate) or permanent (low-dose rate) brachytherapy (BT) with or without additional EBRT. These treatments may be offered independently or in combination with hormonal therapy (androgen deprivation therapy). In recent years, new minimally invasive modalities have emerged and provide alternative treatment options with the most notable being high intensity focused ultrasound (HIFU) and cryosurgery.^{5–7}

EBRT is an effective primary therapy option with good survival rates reported.^{8–10} It is estimated that 12–24% of patients diagnosed with localized prostate cancer receive EBRT as a primary treatment.^{11,12} Although numbers may differ depending on the definition of failure used, in approximately 30% of these patients their cancer will recur^{8,13–16} with some studies reporting even higher rates.^{14,17–20} For patients with local recurrence after EBRT, depending on life expectancy and tumor progression, an alternative (salvage) therapy may still be appropriate in order to limit further progression of the disease and metastasis.^{14,20} The four major options for re-treatment available after EBRT failure are salvage RP, salvage BT, salvage cryosurgery and salvage HIFU.^{15,16,19,21} Amongst these methods, salvage RP is the most established treatment with good oncological outcomes.¹⁵ However, it is associated with high morbidity,^{14–16,18,19,22,23} thus, doctors may be reluctant to recommend it, especially for patients with a short life expectancy.^{14–16,19} The other three modalities provide a less invasive alternative, with HIFU offering the least invasive approach.²⁰

HIFU has been the subject of many studies indicating its potential as a primary treatment for locally confined prostate cancer.²⁴ Accurately determining the efficacy of this modality is not easy, especially due to the inconsistency in reporting biochemical failure and due to the absence of long-term oncological outcomes.^{25,26} As a result and despite already being in use in many centers across the world, HIFU is still classified as an experimental treatment, for example, by the European Association of Urologists (EAU).⁶ Nonetheless, some studies report encouraging results for primary HIFU

treatment with low mortality rate, high metastasis-free survival rate, and acceptable side-effects comparable to other minimally invasive modalities.^{24,26}

Currently, only a limited number of studies report on the efficacy and safety of HIFU as a salvage therapy after failure of EBRT.^{5,15,27} Additionally, no prospective randomized trials have been reported.²⁷ Consequently, comparison of HIFU with other conventional salvage modalities is difficult. Most of the published investigations are retrospective studies,^{14,17,20,28,29} with only a few prospective series reported.^{5,19,23} The majority of these studies report good local cancer control, indicating the potential of HIFU as an effective salvage therapy for low- and intermediate-risk patients. In some studies, the rate of complications reported is high, with some adverse effects comparable to the other salvage therapies. This presents a limitation for the use of HIFU as a salvage therapy.²³ However, it is interesting to observe that in those studies where new refined treatment parameters were introduced, dedicated to post-radiation salvage-HIFU treatments, the side-effects were significantly reduced.^{14,19,23}

Salvage treatment in a previously irradiated prostate is technically challenging, and higher rates and more severe side effects are expected. However, the positive effect of the new treatment parameters introduced in some of the studies for post-EBRT salvage-HIFU demonstrates that there is significant opportunity for improving both the delivery of salvage-HIFU treatment as well as patient selection. An aspect of salvage HIFU that has been overlooked so far, and which may affect the treatment's safety and efficacy as well as patient selection, is the presence of fiducial markers that are increasingly introduced in the prostate as part of modern image-guided radiotherapy (IGRT).^{30,31} To the best of our knowledge, there are no studies investigating the effect of these markers on the delivery of salvage-HIFU after EBRT, with the exception of a small number of studies reporting on the effect of permanent BT seeds on HIFU.^{32,33} The purpose of this work was to perform an extensive quantitative investigation of the effect of fiducial markers on the propagation and focusing of the ultrasound (US) waves when the beam path is obstructed by an EBRT fiducial marker.

The fiducial markers are introduced in the prostate in order to improve the accuracy of EBRT. They facilitate the localization of the prostate, enable motion and deformation tracking and act as reference points for distance measurements as well as for registering images obtained from different imaging modalities.^{30,31,34,35} Typically 3 radio-opaque markers are implanted in the prostate before the patient undergoes EBRT planning and remain permanently in the prostate after the completion of the treatment.^{36,37} The markers are placed within the prostate gland using a transperineal or transrectal approach with a needle holding one or two markers, under the guidance of transrectal ultrasound (TRUS) in a procedure similar to that of a biopsy.^{36,38} Although this may differ between hospitals, the markers are typically placed in the prostate base, mid-gland, and apex at a distance of approximately 2 cm from each other and at least a 15° angle between any fiducial triplets.^{36,39,40} Consequently, only a

single marker is likely to be encountered by the HIFU beam for any individual sonication.

There is a large range of commercially available markers made from a variety of materials in different shapes and dimensions.^{30,34,35,41} The most commonly used markers are made of gold, making them visible in a variety of imaging modalities, and have a cylindrical shape with their surface appropriately shaped to minimize migration.³⁰ Although less frequent, spherical gold markers are also utilized.^{42,43} These two shapes facilitate their insertion using a needle. More recently, new types of markers have emerged that offer some advantages but have yet to gain wide popularity. There are three notable examples. First, carbon fiducials, which offer better visibility and produce less artefacts on computed tomography (CT) images. Second, metallic coils and strings of markers on an absorbable strand, which may offer better stability and localization since they stretch across the whole gland. Finally, a new family of markers with a transponder built-in to allow wireless tracking of their position in real-time without the need for additional imaging of the prostate.³⁰

This work investigates the effect of a single gold marker on the HIFU beam using numerical simulations based on a model of the prostate containing a spherical or cylindrical fiducial. For each marker shape, a series of simulations was performed on a high performance computer (HPC) cluster to evaluate the propagation of the HIFU beam in the prostate when its path is obstructed by a single gold marker. The simulations used the open-source k-Wave^{44,45} toolbox developed by our group for accurate modelling of the propagation of US waves. The simulation results were also used to verify an analytical model developed for approximating the effect of the marker on the intensity at the focus and for identifying a region within which the marker has a significant impact on the focusing. The study was performed in silico for several reasons. First, computer simulations provide an effective and low-cost method for investigating the key factors at play in HIFU therapy delivery in a way that would be impractical, costly, and possibly unethical in patients. Second, simulations give access to a complete characterization of the acoustic field parameters that are not accessible from an experiment. Knowledge of these parameters is critical to understand and quantify the effect of the markers.

2. METHODS

2.A. Clinical HIFU systems for prostate cancer

There are three approved transrectal HIFU treatment systems dedicated to prostate cancer and one transurethral device currently in clinical trials. The transrectal systems are the Sonablate 500 (SonaCare Medical LLC, Charlotte, NC, USA), the Ablatherm II (EDAP TMS, Vaulx-en-Velin, France), and the Focal One also developed by EDAP TMS. The operation of these systems is based on similar principles. They all deliver the treatment using a probe with an integrated HIFU and imaging transducer, which is used

transrectally under US guidance to induce ablation of the targeted region.²⁴ On the other hand, the TULSA-PRO (PROFOUND MEDICAL Corp., Toronto, Canada) delivers transurethral ultrasound ablation of prostate cancer under magnetic resonance imaging (MRI) guidance.⁴⁶

The transducer model used in this work nominally followed the specifications of the Sonablate 500 (SonaCare Medical). This system is currently in use at University College London Hospital (UCLH).⁴⁷ The Sonablate 500 consists of a console, a transrectal probe, and a cooling and degassing module. The transducer is held at the tip of the probe by a motorized system that allows it to move in the longitudinal and transverse direction with a 90 degree treatment window.⁴⁸ The transducer module itself consists of two dual-mode (splitbeam) transducers stacked back-to-back capable of both imaging at 6.3 MHz and treatment at 4 MHz. To achieve this dual-mode operation, each side of the transducer consists of two elements: a circular element at its center, dedicated to imaging, surrounded by an annular element, used for treatment. Each side is manufactured with a different curvature resulting in two fixed focal lengths (30 mm and 40 mm) by means of geometric focusing. This allows the whole prostate gland to be treated using a single probe and without the need for electronic beam steering. The current dimensions of the transducer are 22 mm by 30 mm, noting that earlier revisions of the system used a 22 mm by 35 mm transducer. The dimensions of the earlier revision are followed in this work.

During treatment, the ablation is given in blocks and can be applied to the whole gland or focally to only the cancerous lesion within the prostate. The ablated volume is pseudoellipsoidal and its precise location is determined by the focal length of the transducer. For each sonication, the ablated volume is on the order of $3 \times 3 \times 10 \text{ mm}^3$. Multiple sonications with slight overlap move sequentially through the prostate with 3 s ‘on’ time exposures and 6 s ‘off’ time exposures. The prostate is divided into six blocks, left and right with corresponding anterior, middle, and posterior blocks. The 40 mm focal length is used for anterior and middle block treatment and the 30 mm probe for posterior block treatment. Tissue destruction is produced by thermal, mechanical, and cavitation effects to produce a clearly demarcated region of coagulative necrosis.

2.B. Simulation setup

The simulations were performed using the open-source k-Wave Toolbox.⁴⁴ This solves a generalized version of the Westervelt equation accounting for the combined effects of nonlinearity, heterogeneous material properties, and acoustic absorption following a frequency power law. The transducer geometry was assumed to be a spherical section with width $W_t = 22 \text{ mm}$, length $L_t = 35 \text{ mm}$, focal length $R_t = 40 \text{ mm}$ and without an imaging element included. The simulations were performed using a regular Cartesian mesh and the transducer was defined in the grid as a simply-connected sphere with a single grid-point thickness truncated

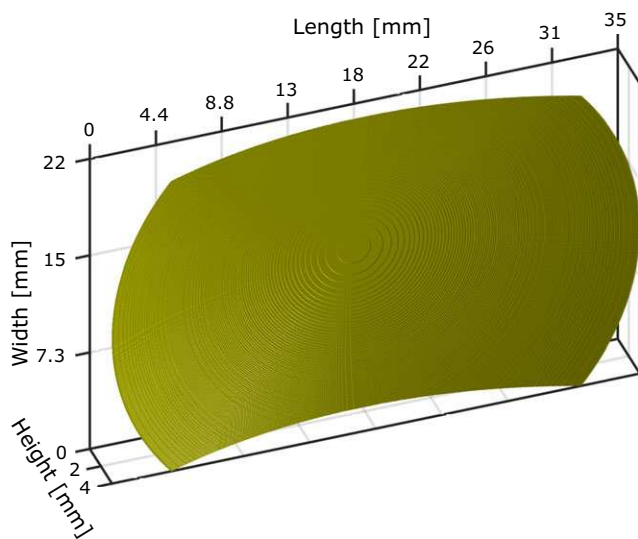


FIG. 1. The discretized transducer model used in the simulations shown in 3D. [Color figure can be viewed at [wileyonlinelibrary.com](#)]

to the appropriate width and height. The discretized transducer model is shown in Fig. 1. The transducer was driven by a $f_0 = 1/T = 4$ MHz sinusoidal input signal, with surface pressure p_0 given by

$$p_0 = \sqrt{2I_{av}\rho_0c_0}. \quad (1)$$

Here ρ_0 and c_0 are, respectively, the density and sound speed of the background medium and $I_{av} = 4$ W/cm² is the time-averaged source surface intensity. The value of I_{av} was selected such that the focal intensity is of the order of magnitude reported for the Sonablate 500 (1000–2000 W/cm²).^{49,50}

The total duration of the input signal was 60 μ s, which was equal to the total simulation time and long enough to ensure the pressure had reached steady-state. To ensure stability, a smaller time step dt was used for the simulations in

which a marker was introduced in the grid.⁴⁵ The time step for the homogeneous case (without marker) was given by $dt = 0.33dx/c_0$, and for the heterogeneous case (with marker) by $dt = 0.066dx/c_0$, where dx is the spatial grid-spacing. As a result, the total number of time steps was 5 times higher for the heterogeneous simulations.

The physical dimensions of the simulation volume were $(L_x, L_y, L_z) = (44.7, 29.4, 60.0)$ mm. This was discretized to a regular Cartesian grid with dimensions (N_x, N_y, N_z) , which included a $L_{PML} = 20$ grid-points (pt) perfectly matched layer (PML) at either end of each coordinate axis.⁵¹ The grid spacing was uniform along all three coordinate axes and was defined according to $dx = dy = dz = L_z/(N_z - 2L_{PML})$. The background medium was assigned the material properties of the prostate (density: $\rho_0 = 1050$ kg/m³ and sound-speed: $c_0 = 1578$ m/s), and the spherical or cylindrical volume occupied by the marker was assigned the properties of gold (density: $\rho_m = 19300$ kg/m³ and sound-speed: $c_m = 3240$ m/s). Reference simulations were also performed without the inclusion of a marker in order to record the characteristics of an uninterrupted HIFU beam. Both sets of simulations were nonlinear (nonlinearity parameter: $B/A = 6.75$) and accounted for absorption following a frequency power law of the form $\alpha_0 f^{y_0}$ where $\alpha_0 = 0.5$ dB MHz^{-y₀} cm⁻¹ and $y_0 = 1.1$.

2.C. Marker placement

To investigate the effect of fiducials on the propagation and focusing of the HIFU beam, each simulation included a single spherical or cylindrical gold marker positioned at different coordinates, with the position of the transducer kept fixed across all simulations. The spherical marker had a 3 mm diameter, whereas the cylindrical had a 3 mm height and 1 mm diameter. The simulated positions for each marker shape are shown in Fig. 2.

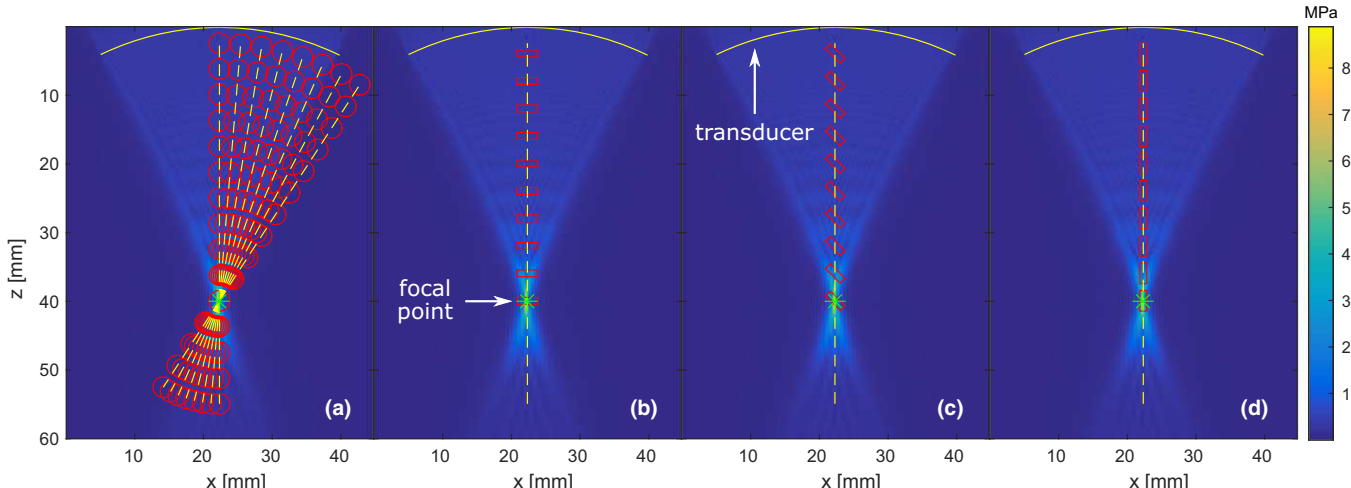


FIG. 2. The positions and orientations simulated for (a) the spherical markers with 3 mm diameter and (b)–(d) the cylindrical markers with 1 mm diameter and 3 mm height. The simulated positions are shown superimposed on the maximum pressure field of a homogeneous medium. The markers were placed on the zx plane which includes the transducer's focal-point \mathbf{m}_f , indicated by the star-like marker. The cross-section of the transducer is also indicated at the top of each figure. [Color figure can be viewed at [wileyonlinelibrary.com](#)]

In order to reduce the number of simulations performed, the center positions of the markers were limited to the xz plane at $y = N_y/2$. This plane includes the center of the focal region which was expected at approximately $\mathbf{m}_f = (N_x/2, N_y/2, \lfloor R_f/d_z \rfloor)$, where \mathbf{m} is a 3-dimensional (3D) vector denoting the coordinates of any point in the grid. If the plane is further divided into four quadrants with the origin at the focal point, the simulated positions were limited to the top-right and bottom-left quadrant as shown in Fig. 2(a). The choice of limiting the tested marker positions into two quadrants on a single plane was based on the assumption that any observed effect will be approximately symmetric about the beam axis. Both types of markers were positioned radially along the axes connecting the focal point to the transducer. The distance between markers along each axis, as well as the angle between successive axes, were kept constant. Hence, the markers can be grouped either with respect to the angle of the radial axis from the beam axis (see Fig. 5(f) inset), or with respect to their distance from the focal-point (see Fig. 5(c) inset).

2.D. Quantifying marker effect

To systematically evaluate the effect of a single marker on the focusing of the HIFU beam, four metrics were selected and evaluated using the simulation results for each marker position. These metrics were later compared to the corresponding quantities obtained from a homogeneous simulation without a marker.

The first quantity evaluated was defined to measure how much the focus has shifted from its intended position. Let \mathbf{m}_{ref} denote the coordinates of the maximum-pressure point extracted from a homogeneous simulation without a marker. This point will be referred as the focal-point, or simply the focus. Let also \mathbf{m}_{max} denote the coordinates of the maximum-pressure point extracted from a heterogeneous simulation with a marker. Then, the focus-shift was calculated using

$$d_{\text{shift}} = \|\mathbf{m}_{\text{max}} - \mathbf{m}_{\text{ref}}\| \quad (2)$$

which is the Euclidean distance between \mathbf{m}_{max} and \mathbf{m}_{ref} .

The next set of metrics were based on the spatial-peak temporal-average (SPTA) intensity (I_{spta}). For each simulated marker position, this quantity was evaluated both at the coordinates of the homogeneous focus (\mathbf{m}_{ref}) and the coordinates of the maximum-pressure point (\mathbf{m}_{max}). The two scalar values ($I_{\text{spta}}(\mathbf{m}_{\text{ref}}) \equiv I_{\text{focus}}$ and $I_{\text{spta}}(\mathbf{m}_{\text{max}}) \equiv I_{\text{max}}$) were obtained using

$$I_{\text{spta}}(\mathbf{m}) = \frac{1}{nT} \int_0^{nT} \frac{p^2(\mathbf{m}, t)}{\rho_0 c_0} dt \quad (3)$$

where $p(\mathbf{m}, t)$ is the pressure time series at the coordinates of the maximum-pressure point ($\mathbf{m} = \mathbf{m}_{\text{max}}$) or the focus ($\mathbf{m} = \mathbf{m}_{\text{ref}}$), $n \geq 1$ is a positive integer and T is the period of the driving frequency. Evaluating Eq. (3) at \mathbf{m}_{ref} for a homogeneous simulation gives the SPTA intensity of an uninterrupted beam denoted as I_{hom} . Comparison of I_{focus} and I_{max} with I_{hom} provides an indication of how much energy is redistributed due to the presence of the marker. It is noted that henceforth intensity will always refer to SPTA intensity.

Finally, to measure how the size of the focal region changes when the marker is included compared to the homogeneous simulation, the -6 dB focal volume was calculated for each simulation. This was obtained using

$$V_f = N dx dy dz \quad (4)$$

where N is the number of voxels for which $I_{\text{spta}}(\mathbf{m})$ was greater than 50% of I_{max} (the maximum intensity for that simulation). As the reference intensity changes for each simulation, this metric does not give a direct indication of the ablation volume. However, taken together with I_{max} , it provides a useful indication of the volume over which the acoustic energy is distributed.

The focusing metrics were evaluated using the final five cycles of the pressure time-series and excluded the pressure time-series recorded within the marker volume. In order to reduce the size of the output from each simulation, the pressure time-series was recorded within a sub-region of the grid (see Table I) centered at the focal-point of the transducer (\mathbf{m}_{ref}). Even with this restriction in place, the output file size was approximately 0.5 TB per simulation.

TABLE I. Computational cost in terms of memory and simulation time associated with each grid-size.

Grid-size (pt^3)	Homogeneous simulations				Time ^c (dd:hh:mm)	Heterogeneous simulations				Time ^c (dd:hh:mm)
	RAM ^a (GB)	Input ^b (MB)	Output ^b (GB)			RAM ^a (GB)	Input ^b (GB)	Output ^b (GB)		
$S_1 = 384 \times 256 \times 512$	10.5	2.9	0.7		00:00:10	11.9	4.1	2.0		00:00:39
$S_2 = 768 \times 512 \times 1024$	37.2	20.3	8.5		00:02:06	48.5	28.3	30.3		00:10:16
$S_3 = 1152 \times 768 \times 1536$	108.4	70.0	37.1		00:12:01	141.7	95.8	144.9		02:13:23
$S_4 = 1536 \times 1024 \times 2048$	246.4	165.2	108.4		01:16:07	331.9	225.9	445.9		08:11:38
$S_5 = 2304 \times 1536 \times 3072$	830.7	554.6	508.7		06:19:51	—	—	—		—

^aRandom access memory (RAM) requirements at each grid-size. MB = 2^{20} bytes, GB = 2^{30} bytes.

^bSize of the input and output files of the simulation. At S_1 the pressure is recorded in the output within a $96 \times 96 \times 192 \text{ pt}^3$ volume. These dimensions increase proportionally to the grid-size, except from S_5 where a smaller volume was used.

^cTime required for completing a single simulation. May vary depending on the HPC's workload. (dd:hh:mm) = (days:hours:minutes).

2.E. Convergence test for grid-size selection

The grid-size required for the simulations was established using a convergence test. In particular, because of nonlinear wave propagation, some of the energy from the fundamental frequency of the driving signal is shifted to higher harmonics. For these harmonics to be captured by the model, the physical domain must be appropriately discretized. For the numerical method used, waves can be accurately propagated close to the Nyquist limit of two grid-points per minimum wavelength. However, the energy at higher frequency harmonics is not known a priori. As a result, the choice of the grid-size will determine the number of harmonics that can be represented on the grid and thus the accuracy with which the nonlinearity is captured. On the other hand, increasing the grid-size translates to higher computational requirements in terms of memory and simulation time. Therefore, the selected grid-size was a compromise between the number of supported harmonics and the associated computational cost.

To determine the appropriate grid-size, homogeneous and heterogeneous simulations were performed at increasing grid dimensions. The configuration of these simulations was as described in Section 2, with the heterogeneous simulation including a single spherical gold marker between the focal-point and the transducer at (0,0,8) mm. Here, the marker position is reported with respect to the coordinates of the focal point. The grid-sizes tested are shown in Table I, noting that a heterogeneous simulation at S_5 was not performed due to the extremely high memory requirements (> 1 TB of RAM). The physical dimensions of the

simulated domain were kept constant as described in Section 2.B. For each simulation the five final cycles of the pressure were extracted at the focal-point. The pressure time-series was then used to evaluate the frequency spectrum and the intensity at the focal-point. The results from the homogeneous convergence test are presented in Fig. 3 (analogous behavior was observed for the heterogeneous set of simulations).

As shown in Fig. 3, by increasing the grid-size, a higher number of harmonics is supported and the effects of nonlinear propagation are more accurately captured. At the lowest grid-size S_1 only the fundamental frequency is supported, thus, the pressure waveform is a pure sinusoid but with a reduced amplitude. As the grid-size increases, the higher frequencies supported capture the nonlinear steepening of the wave and the amplitude of the pressure waveform increases. As the grid-size increases the pressure waveform also converges. Beyond the 6th harmonic (24 MHz), which is close to the maximum frequency supported by S_4 , the amplitude of the higher harmonics becomes extremely small in comparison to the fundamental frequency. Also, the intensity at S_5 changes only by 1.79% from its value at S_4 . On the other hand, the computational cost increases dramatically when switching to S_5 (~ 7 days vs. ~ 2 days) making multiple simulations impractical even on the large computing cluster used for this study. Having in mind the trade-offs described here, the remaining simulations were performed at S_4 . It is noted that, with more than 10 billion grid points, the simulation at S_5 is one of the largest ultrasound simulations of its kind performed to date.⁵²

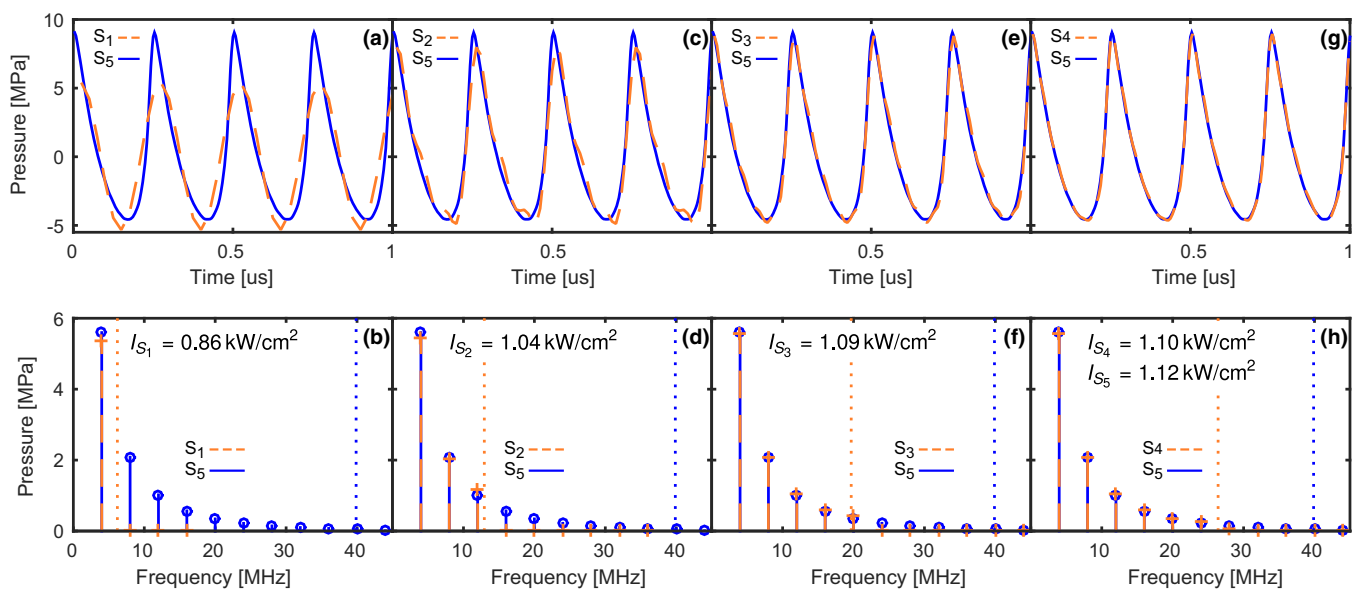


Fig. 3. Results of the convergence test performed in a homogeneous medium for selecting the appropriate grid-size of the simulations. The first row [(a), (c), (e) and (g)] shows the pressure time series at the focal-point and the second row [(b), (d), (f) and (h)] shows the respective frequency spectrum for each time series together with the SPTA intensity calculated using the time series. Each pair of plots compares the time and frequency response at a lower grid-size with the respective response at the highest grid-size S_5 simulated in this study. The grid dimensions are detailed in Table I. The vertical dotted lines indicate the maximum supported frequency at the corresponding grid-size. As the grid-size increases, a higher number of harmonics is supported and the effects of non-linear propagation are more accurately captured by the model. [Color figure can be viewed at wileyonlinelibrary.com]

2.F. Simulation deployment

The simulations were performed using the MPI version of k-Wave^{52,53} on the IT4Innovations' Salomon HPC based at the National Supercomputing Center at VSB-Technical University of Ostrava in the Czech Republic. The actual hardware utilized for each simulation comprised of 144 cores and 768 GB of RAM (6 nodes with two Intel Xeon E5-2680v3 processors, each equipped with 24 cores and 128 GB RAM, interconnected by a 7D Enhanced hypercube Infiniband network). For the S_5 simulation, 9 nodes were utilized. Table I summarizes the memory and simulation-time requirements for a single homogeneous and heterogeneous simulation at each grid-size. At S_4 , the output of a single heterogeneous simulation was 445.9 GB. With a total of 143 marker positions tested, the simulations generated ~ 63 TB of output data and required ~ 5 million core-hours to run. After the completion of the simulations, the output data was processed in Matlab to evaluate the various metrics quantifying the effect of the marker as described in Section 2.D.

3. SIMULATION

A total of 143 marker positions were simulated: 113 with a spherical marker and 30 with a cylindrical marker at three orientations. Figure 4 provides a visual description of the simulations performed to determine the marker effect on the HIFU beam. Figure 4(a) shows the maximum pressure field as recorded across the whole domain when the HIFU beam propagates in a homogeneous medium. The inset is a visualization of the -6 dB focal volume. The metrics extracted from this simulation serve as a reference for comparison to assess how placing a marker in the path of the beam deteriorates the focusing. Figure 4(b)–4(d) demonstrate how the maximum pressure field and the focal volume changes when a marker is introduced and gradually moved away from the

focal-point. Figure 4(b) shows the dramatic effect of the marker when placed very close to the focal-point, while Figs. 4(c)–4(d) illustrate how the marker effect decreases as its distance from the focal-point increases. Finally, Fig. 4(d) shows that beyond a certain distance, focusing is re-established with the marker effect becoming less pronounced.

The metrics extracted for each marker position can be used to quantitatively study the marker's effect. Figures 5 and 6 show the evaluated metrics for the spherical and cylindrical gold markers respectively. For both sets of plots, the metrics are plotted along the axes connecting the focal-point to the transducer. The metrics are plotted with respect to the distance of the marker from the focal-point, with the positive direction indicating that the marker is positioned toward the transducer.

Figures 5(a) and 5(b) show how the intensity (which is proportional to the rate of heat deposition) changes with marker position at the maximum-pressure point (\mathbf{m}_{\max}) and at the focus (\mathbf{m}_{ref}), respectively. When the spherical marker is positioned very close to the focus, the intensity reduces dramatically. However, as the marker moves away from the focal-point and towards the transducer, the intensity increases. As an indication, at 11.5 mm and 8.5 mm the intensity at the focal-point is reduced by 10% and 20% respectively. Moving the marker further away from the focus, both intensities continue to gradually increase and eventually converge to approximately I_{hom} , indicating that focusing has been re-established fully.

A slightly different behavior is observed when the marker is positioned at exactly the focus (\mathbf{m}_{ref}) of the transducer. It is clear from Fig. 5(b) that practically no energy reaches the intended focal position. On the other hand, Fig. 5(a) shows that the maximum intensity more than doubles due to the reflections caused by the marker, which redirect the energy to the pre-focal region. This is due to the large impedance difference between the background medium (prostate) and the

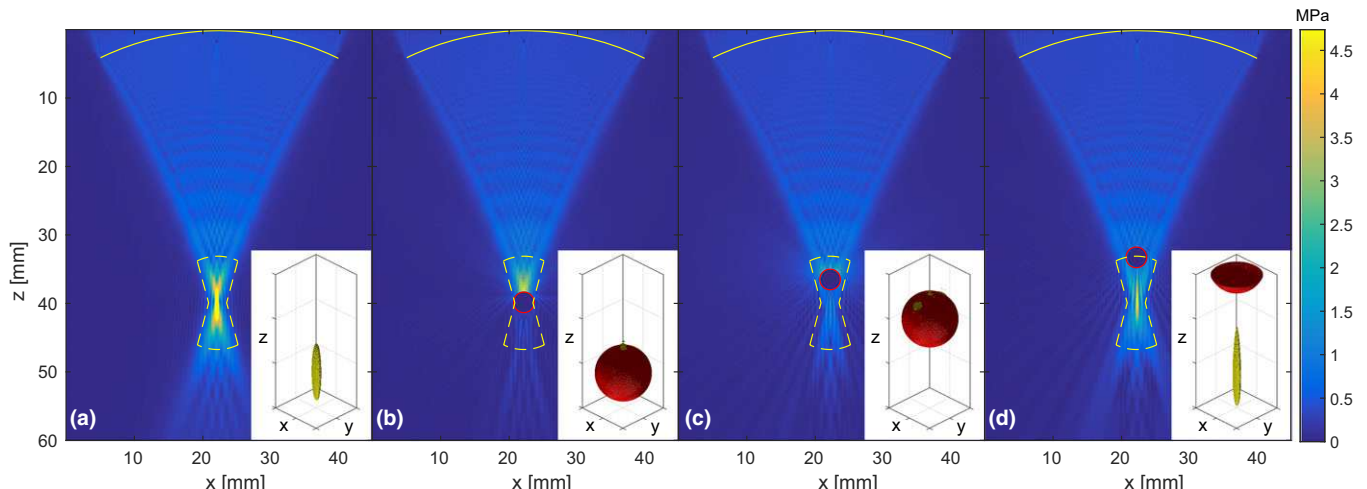


FIG. 4. Maximum pressure field of (a) a homogeneous simulation and (b)–(d) three heterogeneous simulations for three marker positions. The insets have dimensions $3 \times 3 \times 8$ mm and are visualizations of the -6 dB focal-volume (dashed outline) evaluated using Eq. (4) and the spherical marker (solid-line circle). For each marker position, the metrics in Section 2.D. were evaluated and compared with the corresponding reference values of the homogeneous simulation. When the marker is inside the region indicated by the dashed line, the intensity at the focus drops by more than 30%. [Color figure can be viewed at wileyonlinelibrary.com]

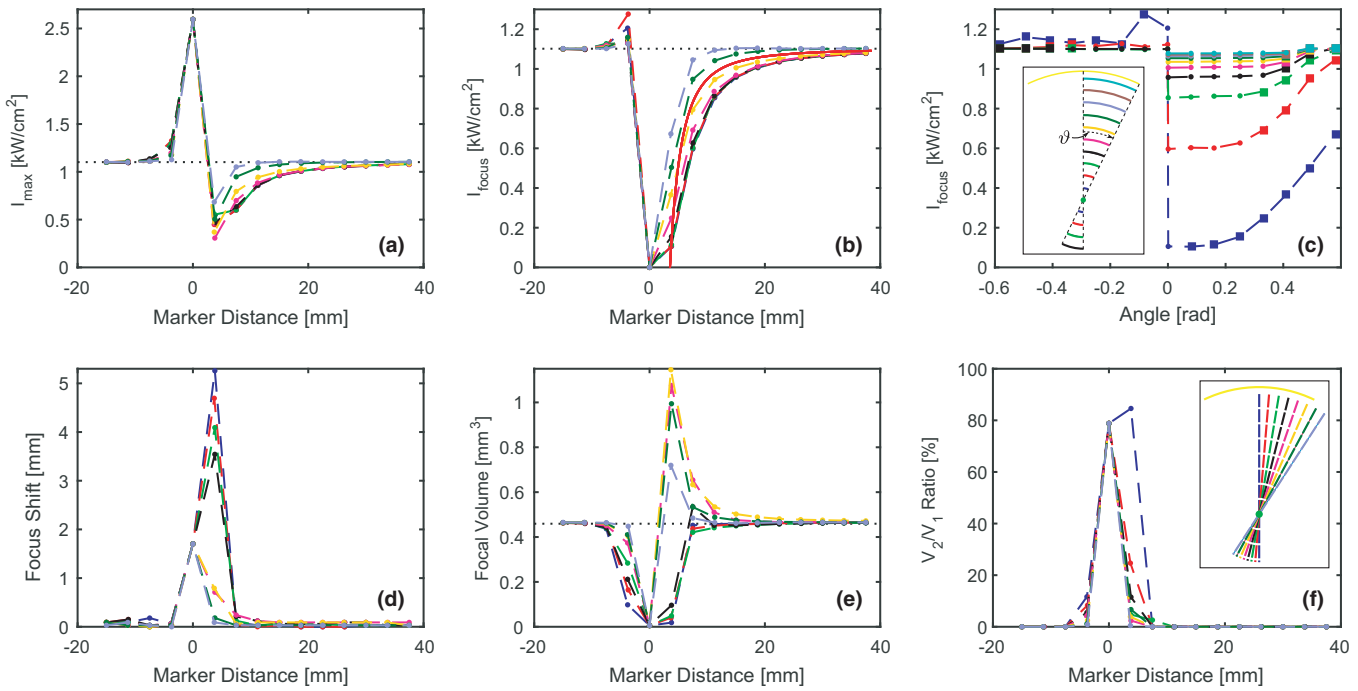


FIG. 5. Metrics quantifying the effect on the HIFU beam of a 3 mm gold spherical marker. All the metrics, except in (c), are plotted with respect to marker distance from the focus, with each curve corresponding to one of the radial axes shown in the inset of (f). The horizontal dotted line corresponds to the respective metric value obtained from a homogeneous simulation. (a) and (b) show respectively the intensity evaluated using Eq. (3) at the maximum-pressure point (\mathbf{m}_{\max}) and at the focus (\mathbf{m}_{ref}), with the solid-line in (b) showing the intensity as predicted by the geometric model in Eq. (5). (d) shows how the distance between \mathbf{m}_{\max} and \mathbf{m}_{ref} changes as calculated with Eq. (2). (e) is the focal-volume with marker position as given by Eq. (4) and (f) is the ratio between the second (V_2) and first (V_1) largest volumes in the focal region. Finally, (c) shows the intensity at the focus but plotted against the angle (ϑ) between the central radial axis and the axis on which the marker lies. Here, each curve corresponds to the group of markers at a constant distance from the focus as indicated in the inset. [Color figure can be viewed at wileyonlinelibrary.com]

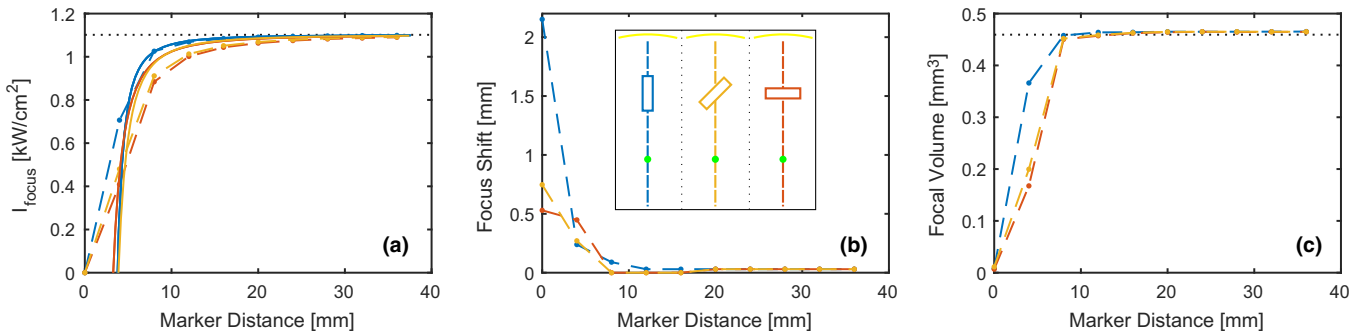


FIG. 6. Metrics quantifying the effect on the HIFU beam of a 3×1 mm gold cylindrical marker at different orientations. All the metrics, are plotted with respect to marker distance from the focus, with each curve corresponding to one of the orientations shown in the inset of (b). The horizontal dotted line corresponds to the respective metric value obtained from a homogeneous simulation. (a) is the intensity at the focus (\mathbf{m}_{ref}) given by Eq. (3), with the solid-lines showing the intensity as predicted by the geometric model in Eq. (5) for each orientation. (b) is the change in the distance between \mathbf{m}_{\max} and \mathbf{m}_{ref} evaluated using Eq. (2) and (c) is the focal-volume with marker position as given by Eq. (4). [Color figure can be viewed at wileyonlinelibrary.com]

marker (gold), which results in a high reflection coefficient ($R = 0.91$). When the marker is gradually shifted in the negative direction, the intensity at the maximum I_{\max} and the focus I_{focus} quickly converge to the homogeneous value I_{hom} with no significant reflections observed beyond approximately -4 mm.

Figure 5(d) illustrates the effect of the marker on the position of the maximum pressure (\mathbf{m}_{\max}) relative to the focal-point (\mathbf{m}_{ref}). When the marker is positioned at a distance between -4 mm and 8 mm from the focal-point, a

shift in the focus is observed of up to approximately 5.5 mm. The distortion caused by the marker can also be observed by looking at the variation in the size of the focal volume in Fig. 5(e) and the insets in Fig. 4. When the marker is placed at a distance from the focus between -4 mm and 8 mm, the focal volume decreases as its position moves closer to the focal-point, indicating its negative effect on the beam. The markers placed along the four outer radial axes seem to diverge from this behavior. As those markers move towards the focus from the positive

direction, the decrease in focal volume is first preceded by a sharp increase. This is likely due to refocusing caused by reflections and diffraction around the marker. Moving the marker beyond -4 mm and 8 mm causes the focal volume to gradually converge back to its homogeneous value, indicating that focusing is re-established.

Placing the marker close to the focus also causes the focal-volume to split from a single region [Fig. 4(a)] into multiple smaller volumes of high pressure [Fig. 4(b)], which may induce heating at undesired locations. Figure 5(f) shows the ratio between the second (V_2) and first (V_1) largest connected components of the -6 dB volumes for each marker position. The ratio between the two volumes increases as the marker is positioned closer to the focus. When the marker is placed away from the focal-point the size of V_2 reduces to zero demonstrating that any secondary regions of high pressure are eliminated.

Figure 5(c) offers an alternative perspective on the effect of the marker on the intensity at the focus. In this case, the markers are grouped together with respect to their distance from the intended focus. Therefore, each curve corresponds to a fixed distance from the focus. The intensity is plotted with respect to the angle between the z -axis passing through the focus and the radius connecting the center of the marker with the focus. The markers outside the HIFU beam are denoted with squares whereas those inside the beam are denoted with dots. This plot shows that, as long as the marker is positioned inside the HIFU beam, its effect on the intensity remains approximately the same when its distance from the intended focus is kept constant. The figure also demonstrates the large reduction in intensity due to the markers closer to the focus (positive angles), however, as the angle increases, their effect on the intensity reduces since they move outside the HIFU beam. For the markers beyond the focus (negative angles), a small increase in intensity can be seen which reduces as their distance from the focus increases in the negative direction. The analogous behavior is observed for the focus shift and focal volume.

To investigate the effect of marker shape, another set of simulations was performed using a single gold cylindrical marker. A total of 30 simulations were executed: 10 marker positions were simulated along the z -axis passing through the focal-point with 3 orientations for each position as shown in Fig. 2(b)–2(d). The orientation in Fig. 2(b) is the most likely to be encountered in practice because of the procedure with which the markers are inserted. The simulations were restricted to a single radial axis in order to limit the number of simulations executed. This restriction was justified based on the observation that the effect of the spherical marker remains constant at a fixed distance from the focal-point as demonstrated in Fig. 5(c).

For each position of the cylindrical marker, the same set of metrics were calculated. Comparison of the plots in Fig. 6 with the corresponding plots in Fig. 5 suggests that the cylindrical marker distorts the HIFU beam in the same manner as the spherical marker. Namely, as the marker moves closer to

the focal-point, the intensity and focal-volume decrease while the shift in the focus increases. It is also interesting to observe that marker orientation has an effect. For example, in terms of the intensity at the focal-point, the orientation parallel to the beam's axis has the smallest impact since the surface area encountered by the wave is the smallest, but it has the largest focus shift since the maximum pressure point occurs close to the base of the marker furthest from the focus. For the remaining two orientations, the metrics in Fig. 6 vary in a similar manner. This is likely due to their projected areas on the HIFU beam being similar.

4. GEOMETRIC MODEL

The results discussed above suggest that the distortion introduced by the marker is dominated by strong reflections. This is not surprising due to the large density difference between the background medium and gold, which results in a high reflection coefficient at the interface of the two materials. Additionally, the impact of the different marker orientations suggests a dependence on the surface area of the marker encountered by the wave. Based on these observations and with the aim of providing a faster and more efficient method for estimating the effect of different markers, a simple analytical model was derived which evaluates the focal intensity by considering the effect of a single marker.

Figure 7 defines the various parameters of the model assuming a spherical marker. More specifically, it shows the HIFU beam of the geometric model (solid-yellow line), whose size is determined by the focal length of the transducer R_t , its width W_t and its length L_t . Figure 7 also shows a cross-section of the beam with a spherical-strip shape (solid-green line), which is tangential to the point on the marker furthest from the focus. The cross-section has a length L_w and width W_w with a radius R_w . The circle indicates a cross-section of the spherical marker with diameter d and its center at a distance r from the focal-point. It is noted that, although a spherical marker is considered as an example here, the model can be adapted to any other shape.

With reference to Fig. 7, let I_{hom} denote the intensity at the focal-point of an uninterrupted beam (evaluated from a homogeneous simulation), A_w the total area of the beam's cross-section and A_m the projected area of the marker on the cross-section (red-solid line). Then, the intensity at the focus (\mathbf{m}_{ref}) when the beam is obstructed by a marker is approximately given by

$$I_{\text{focus}} \approx I_{\text{hom}} \left(1 - \frac{A_m}{A_w} \right). \quad (5)$$

The values of A_m and A_w vary according to the distance of the marker from the focal-point. Additionally, A_m changes depending on the marker's shape and its orientation. Thus, evaluating Eq. (5) requires a single homogeneous simulation to obtain I_{hom} and then calculation of the areas A_m and A_w . This is a significant improvement in terms of computation time since, after obtaining I_{hom} from a single homogeneous simulation, the time required for evaluating Eq. (5) is

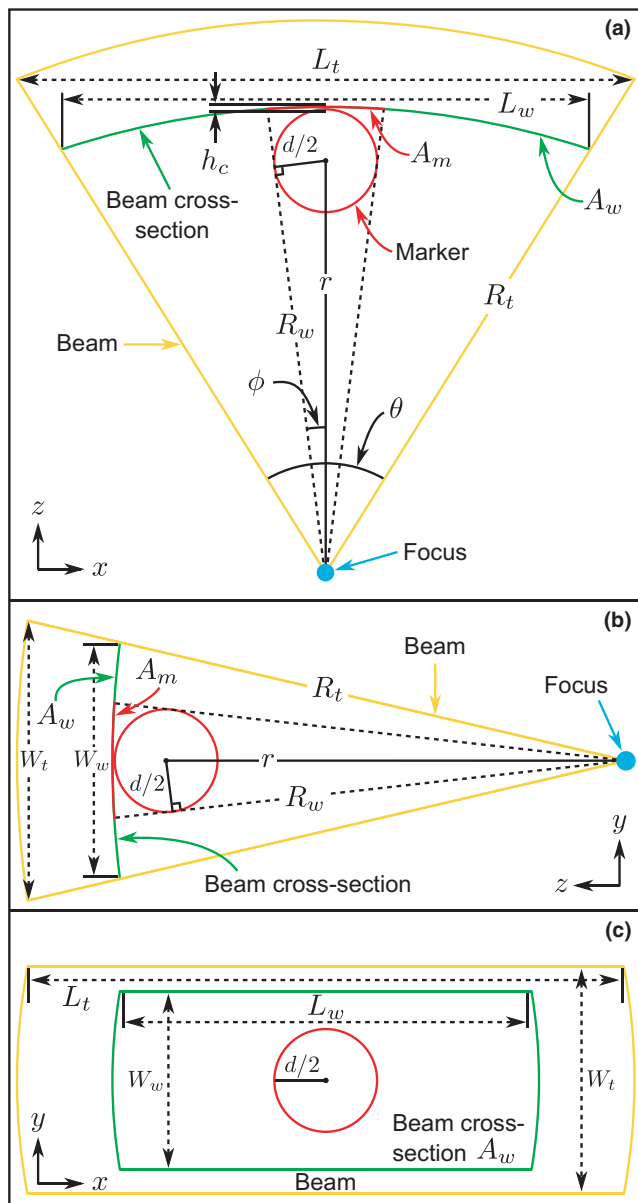


FIG. 7. The parameters of the geometric model defined in Eq. (5) assuming a spherical marker. The parameters are shown on (a) the xz, (b) the yz and (c) xy planes. [Color figure can be viewed at wileyonlinelibrary.com]

negligible compared to simulations. The model omits wave propagation due to diffraction or refraction and accounts only for perfect reflection. It also assumes that the energy lost only depends on the shape of the marker, its distance from the transducer's focus and the shape of the cross-section of the beam tangential to the marker.

The total area of the beam's cross-section A_w can be approximated as the area of a sector of a spherical strip

$$A_w = \theta R_w W_w \quad (6)$$

where θ is the angle defining the sector of the strip in radians, W_w is the width of the strip and R_w is the radius of the sphere on which the strip lies. As shown in Fig. 7, in this example $\theta = 2 \arcsin(L_t/(2R_t))$ and $R_w = r + d/2$, since a

spherical marker is assumed here, and $W_w = R_w W_t/R_t = (r + d/2)W_t/R_t$. Substituting in Eq. (6) yields

$$A_w = \frac{2W_t(r + d/2)^2 \arcsin(L_t/(2R_t))}{R_t}. \quad (7)$$

Calculating A_w for a different marker shape only requires obtaining a value for R_w with the rest of the steps remaining unchanged.

For a spherical marker, its projected area A_m on the tangential cross-section of the beam, as indicated in Fig. 7 (red solid line), has a spherical-cap shape whose surface area is given by

$$A_m = 2\pi R_w h_c \quad (8)$$

where R_w is the radius of the sphere on which the spherical cap lies and h_c is the cap's height. In this example, $R_w = r + d/2$ as explained above and $h_c = R_w - R_w \cos \phi$, where $\phi = \arcsin(d/(2r))$. Substituting in Eq. (8) then gives

$$A_m = 2\pi \left(r + \frac{d}{2} \right)^2 \left[1 - \cos \left(\arcsin \left(\frac{d}{2r} \right) \right) \right]. \quad (9)$$

Analogous arguments hold for evaluating the projected area A_m for the cylindrical marker, or any other marker shape.

The effect of both the spherical and cylindrical marker on the intensity at the focal-point as predicted by Eq. (5) is compared with the simulation results in Figs. 5(b) and 6(b) respectively (denoted by the solid-lines). To quantify the agreement of the model with the simulated intensity at the focus (I_{focus}), the root-mean-square relative error (RMSRE) was evaluated along the beam axis to which the other axial responses converge to and it is shown in Table II. The model slightly underestimates the marker's effect and becomes less accurate for marker positions closer to the focus, but overall it confirms the assumption that

TABLE II. Exclusion zone radius evaluated using the geometric model defined in Eq. (5) for different types of markers and orientations.

Marker type	Dimensions (mm) ^a	Orientation (degrees) ^b	Distance (mm) ^c	RMSRE (%) ^d
Spherical	1	—	2.3	—
Spherical	2	—	4.5	—
Spherical	3	—	6.8	15.7
Cylindrical	3×1	0°	5.0	8.1
Cylindrical	3×1	45°	5.7	18.2
Cylindrical	3×1	90°	5.3	22.8

^aDimensions are: diameter for spherical marker, height × diameter for cylindrical marker.

^bAngle measured on xz plane between the central radial axis connecting the focus to the transducer and the symmetry axis of the cylinder.

^cThe distance from the focal-point towards the transducer at which the intensity drops by 30%, which is equivalent to approximately a 50% reduction in lesion volume, calculated using Eq. (5).

^dRoot-mean-square relative error (RMSRE) of the intensity at the focus (I_{focus}) between the simulated values along the beam axis and those evaluated using the geometric model.

reflections are the dominating effect causing the observed distortion. This suggests that Eq. (5) can be used to approximate the marker effect for arbitrary shapes without the necessity of performing time-consuming and computationally intensive simulations.

Table II provides an indicative list of distances from the focal-point at which the intensity drops by 30%, which is equivalent to approximately a 50% reduction in lesion volume, for different dimensions of cylindrical and spherical markers. The listed distances were evaluated using the analytical model in Eq. (5). Considering that the effect of a marker within the ultrasound beam remains the same at a fixed distance from the focal-point, Table II may be used to define a region around the focal-point within which the marker's impact on the beam is significant and thus may affect the delivery of the HIFU treatment. An example of such an *exclusion zone* is shown in Fig. 4(a) for the 3 mm spherical marker, where the radius of the exclusion zone from the focus was extracted from Table II and its lateral width was evaluated using four times the beam width ($4 \times 1.41c_0/f_0R_t/L_t \approx 2.6$ mm). The region defined by these boundaries may be used to evaluate whether a particular region in the prostate can be effectively treated using transrectal HIFU when a marker obstructs the beam.

5. CASE STUDIES

The results presented in the previous sections suggest that the marker distorts the HIFU beam with its effect increasing the closer it is positioned to the focus. To examine how these results might be applied in a clinical setting, four datasets have been retrospectively selected of patients with recurrent prostate cancer after failed EBRT, which were eligible for salvage-HIFU at UCLH. Three cases were selected in which the presence of the marker may affect the treatment and one case in which the marker is not expected to impose any risk. As shown in Fig. 8, for each patient three images from different modalities are presented co-registered. In each of these images, a contour identifies the region targeted during the treatment and a dot indicates the assumed position of a 3×1 mm cylindrical marker. Due to the difficulty in locating the exact marker position of the medical images, the marker positions were added in software retrospectively based on standard insertion protocols. The outline of the exclusion zone is also shown with its radius extracted from Table II for the cylindrical marker at 45° and its orientation determined by the likely direction of propagation of the HIFU beam indicated by the dashed line. Table III provides details of the four case-studies including the post-operative outcome with regards to any recurrence and its position for comparison with the modelled outcome.

For the first patient, the marker is close to the rectal wall and inside the region targeted during the treatment. Having in mind the strong reflections induced when positioned close to the focus, the marker may cause two side-effects. Firstly, the reflected wave may cause secondary

regions of high pressure on the rectal wall, and secondly, the region in the top part of the exclusion zone may not receive enough energy to be adequately treated. Reviewing the patient's post-operative outcome confirmed (Table III), a recurrence in the lateral position of the lesion consistent with possible disruption from the position of the fiducial marker. In the second example, the marker is positioned near the upper edge of the region to be treated. In this case, the reflections due to the marker may cause excessive heating of regions in the bottom part of the exclusion zone, although this is unlikely to affect overall treatment efficacy. The clinical outcome was once again consistent with the modelling outcome. Although the patient developed a recurrence it was in the midline, some distance away from the marker, and thus the recurrence is likely due to either an inadequate surgical margin taken during the HIFU treatment or due to incomplete cell kill. The third patient, demonstrates another extreme case in which the marker is positioned near the lower bound of the treatment area. Here the reflected wave may induce heating in areas outside the desired treatment region within the bottom part of exclusion zone and leave the top part of the exclusion zone inadequately treated. In this case, recurrence of the tumor was again observed which, although not entirely in the predicted field of recurrence, it may have been influenced by the presence of the marker. In the final example, the marker is positioned away from the intended treatment region, thus, it is not expected to affect the treatment. This is confirmed by the post-HIFU MRI with no residual tumor within the treatment zone.

6. SUMMARY AND DISCUSSION

Gold fiducial markers are commonly used as part of the IGRT procedure during EBRT for men with localized or locally advanced prostate cancer. These markers remain permanently implanted in the prostate. Thus, they may affect the efficacy and safety of the subsequent use of HIFU treatment as a salvage therapy in case of local cancer recurrence. This work investigated the impact on the HIFU beam of a single spherical or cylindrical gold fiducial marker through a series of simulations performed using the open-source k-Wave Toolbox. For each marker configuration, four metrics were evaluated to quantify its impact on the beam. By comparing these metrics with their corresponding values from a homogeneous simulation, it is evident that the distortion introduced by the marker increases as its distance from the transducer's focus decreases and depends on the marker's shape.

Assuming perfect reflections, an analytical model was developed based on geometric arguments, which estimates the impact of the marker on the intensity at the focus. Using the model, which is in good agreement with the simulated results, it is possible to identify the boundaries of a region around the focus within which the presence of a marker will lead to an intensity drop below an acceptable threshold. For

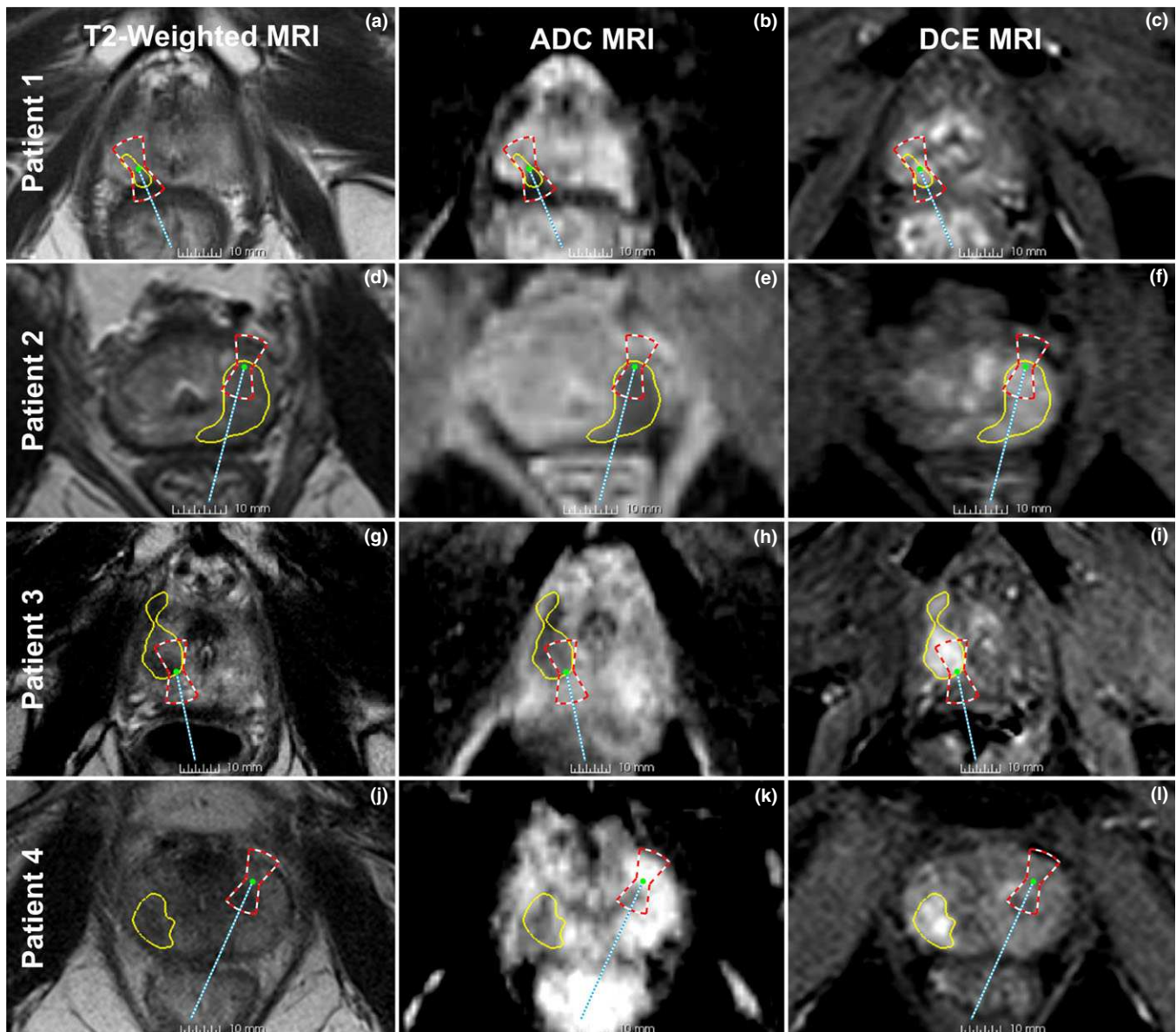


Fig. 8. Diagnostic images of four prostate-cancer patients. From left to right, the images are T2-weighted, apparent diffusion coefficient (ADC), and dynamic contrast enhanced (DCE) magnetic resonance images (MRI). For each patient the three images are co-registered and show the targeted treatment region (solid-line contour), the position of a 3×1 mm cylindrical gold marker (dot marker), the exclusion zone (dashed outline) for a cylindrical marker at 45° and the direction of propagation of the HIFU-beam (dashed straight line). The exclusion zone is positioned such that the focus of the transducer coincides with the position of the marker and it is aligned with the direction of propagation of the HIFU beam. [Color figure can be viewed at wileyonlinelibrary.com]

TABLE III. Clinical characteristics of the patients with recurrent prostate cancer after failed EBRT included in the case study.

Case	Cancer stage	Location ^a	Lesion volume	Salvage HIFU treatment plan	Outcome	Possible marker effect
Case 1	Intermediate risk Gleason 3+4 prostate cancer	Right PZ apex	1 cc	Quadrant ablation, 4 cm and 3 cm blocks	Infield failure - lateral recurrence	Yes
Case 2	Intermediate risk Gleason 3+4 prostate cancer	Left PZ mid to apex extending across midline	2.3 cc	Extended left hemi-ablation	HIFU infield failure - midline recurrence at edge of treatment zone	No
Case 3	Intermediate risk Gleason 3+4 prostate cancer	Right PZ	1.1 cc	Right subtotal hemi-ablation in 4 cm, 3 cm and 3 cm blocks	Infield failure at site of marker	Yes
Case 4	Intermediate risk Gleason 3+4 prostate cancer	Right anterior TZ	0.8 cc	Right quadrant ablation in 4 cm and 3 cm blocks	No recurrence	No

^aPZ: peripheral zone, TZ: transitional zone.

example, as shown in Table II, placing a 3×1 mm marker within approximately 5 mm of the focus in the pre-focal region will induce an intensity drop of more than 30% of the homogeneous value, which will cause a reduction in the volume of the ablated region. As examined in Fig. 8 using scans of prostate cancer patients, this region around the marker can be divided into two parts: an undertreated region due to less energy arriving above the focus and an overtreated region due to reflections below the focus. Both effects may be undesirable depending on the location of the marker. Moreover, there is evidence that the region of recurrence after EBRT is the main tumor (index lesion).⁵⁴ Therefore, the results of this study may justify avoiding the index lesion during fiducial marker placement. Although a degree of accuracy was observed between the position of the marker and the site of recurrence, the cohort consisted only of four patients, thus extracting firm conclusions is difficult. Further work using larger retrospective and prospective cohorts is necessary to further develop and validate the model to allow its utilization in clinical practice. Such a study will aim to reveal the percentage of affected patients by the results of this study and whether the marker's impact can justify the exclusion of some patients from salvage-HIFU or the revision of the placement protocol of fiducial markers during EBRT. Experimental measurements on ex vivo tissue phantoms with implanted markers are also needed to confirm these results.

While investigating the distortion introduced by the marker, the study has omitted some additional factors which may affect the significance of the marker's impact on the treatment. Firstly, as discussed in Section 2.A., the Sonablate 500 probe, on which the transducer model was based, includes an imaging transducer which was not taken into account in the simulations. Although this is expected to affect the intensity at the focus (for the same source surface intensity), it is unlikely to change the distortion introduced by the marker. Similarly, since the operation of the other existing transrectal and transurethral HIFU systems is based on the same principles, using a different transducer model is not expected to affect the behavior of the marker observed here. Second, only the effect on the intensity at the focus (which correlates with heating rate) has been investigated. However, in practice, additional heating may occur due to absorption within the marker and viscous relative motion between the marker and surrounding tissue. These effects, combined with the multiple sonications used during a treatment, may help to counteract the reduced heating due to the lower intensity. It is also unclear from this work whether cavitation, which is triggered by large negative pressures, is reduced due to the presence of the marker. Finally, although other types of markers exist (see Section 1), only gold markers have been considered. However, given that all the materials used have greater impedance than the prostate, using other types of markers is unlikely to change the behavior observed here. A scenario in which the treatment may be severely affected is when a large number of marker-like elements are introduced in the prostate. Such a situation occurs during salvage-HIFU after failed (low-dose) brachytherapy,

where a large number of seeds are permanently implanted in the prostate. Extending the insights of this work for the brachytherapy case and exploring other factors which may affect the distortion introduced by the marker, will be the subject of future work.

ACKNOWLEDGMENTS

This work was supported by the Engineering and Physical Sciences Research Council (EPSRC) in the United Kingdom, grant numbers EP/L020262/1 and EP/M011119/1. Computational resources were supported by the Partnership For Advanced Computing in Europe (PRACE, PROS-HIFU), IT4Innovations National Supercomputing Center, and the UCL Legion High Performance Computing Facility (Legion@UCL). We acknowledge that the results of this research have been achieved using the PRACE-3IP project (FP7 RI-312763) resource Supernova based in Poland at the Wroclaw Center for Networking and Supercomputing. This work was also supported by The Ministry of Education, Youth and Sports, Czech Republic from the Large Infrastructures for Research, Experimental Development and Innovations project "IT4Innovations National Supercomputing Center - LM2015070". Jiri Jaros is financed from the SoMoPro II Programme, co-financed by the European Union and the South-Moravian Region. This work reflects only the author's view and the European Union is not liable for any use that may be made of the information contained therein. Eli Gibson was supported by a Postdoctoral Fellowship awarded by the Canadian Institute for Health Research (CIHR). We thank Dr. Naren Sanghvi of SonaCare Medical LLC for providing technical details on the Sonacare 500 HIFU device.

CONFLICT OF INTEREST

The authors have no relevant conflicts of interest to disclose.

^{a)}Author to whom correspondence should be addressed. Electronic mail: p.s.georgiou@ucl.ac.uk.

REFERENCES

1. Ferlay J, Soerjomataram I, Ervik M, et al. GLOBOCAN 2012 v1.0, Cancer Incidence and Mortality World-wide: IARC CancerBase No. 11, 2013.
2. European Cancer Observatory (ECO). Cancer Fact Sheets, 2016.
3. American Cancer Society. Cancer Statistics Center, 2016.
4. Torre LA, Bray F, Siegel RL, Ferlay J, Lortet-Tieulent J, Jemal A. Global cancer statistics, 2012. *CA: Cancer J Clin.* 2015;65:87–108.
5. Warmuth M, Johansson T, Mad P. Systematic review of the efficacy and safety of high-intensity focussed ultrasound for the primary and salvage treatment of prostate cancer. *Eur Urol.* 2010;58:803–815.
6. Mottet N, Bellmunt J, Briers E, et al. EAU - ESTRO - SIOG Guidelines on Prostate Cancer, Tech. Rep. 2016.
7. Thompson I, Thrasher JB, Aus G, et al. Guideline for the management of clinically localized prostate cancer: 2007 update. *J Urol.* 2007;177: 2106–2131.

8. Borghede G, Aldenborg F, Wurzinger E, Johansson K-A, Hedelin H. Analysis of the local control in lymph-node staged localized prostate cancer treated by external beam radiotherapy, assessed by digital rectal examination, serum prostate-specific antigen and biopsy. *BJU Int.* 1997;80:247–255.
9. Boorjian SA, Karnes RJ, Viterbo R, et al. Long-term survival after radical prostatectomy versus external-beam radiotherapy for patients with high-risk prostate cancer. *Cancer.* 2011;117:2883–2891.
10. Grimm P, Billiet I, Bostwick D, et al. Comparative analysis of prostate-specific antigen free survival outcomes for patients with low, intermediate and high risk prostate cancer treatment by radical therapy. Results from the prostate cancer results study group. *BJU Int.* 2012;109:22–29.
11. Punnen S, Cowan JE, Chan JM, Carroll PR, Cooperberg MR. Long-term Health-related Quality of Life After Primary Treatment for Localized Prostate Cancer: Results from the CaPSURE Registry. *Eur Urol.* 2015;68:600–608.
12. National Cancer Intelligence Network, Treatment routes in prostate cancer: urological cancers SSCRG. Tech. Rep. (NCIN) 2012.
13. Zelefsky MJ, Reuter VE, Fuks Z, Scardino P, Shippy A. Influence of local tumor control on distant metastases and cancer related mortality after external beam radiotherapy for prostate cancer. *Journal Urol.* 2008;179:1368–1373.
14. Murat F-J, Poissonnier L, Rabilloud M, et al. Mid-term results demonstrate salvage high-intensity focused ultrasound (HIFU) as an effective and acceptably morbid salvage treatment option for locally radiorecurrent prostate cancer. *Eur Urol.* 2009;55:640–649.
15. Kimura M, Mouraviev V, Tsivian M, Mayes JM, Satoh T, Polascik TJ. Current salvage methods for recurrent prostate cancer after failure of primary radiotherapy. *BJU Int.* 2010;105:191–201.
16. Shoji S, Nakano M, Omata T, et al. Salvage high-intensity focused ultrasound for the recurrent prostate cancer after radiotherapy. *AIP Conference Proceedings.* 2010;1215:234–238.
17. Agarwal PK, Sadetsky N, Konety BR, Resnick MI, Carroll PR. Treatment failure after primary and salvage therapy for prostate cancer. *Cancer.* 2008;112:307–314.
18. Touma NJ, Izawa JI, Chin JL. Current status of local salvage therapies following radiation failure for prostate cancer. *J Urol.* 2005;173:373–379.
19. Berge V, Baco E, Karlsen SJ. A prospective study of salvage high-intensity focused ultrasound for locally radiorecurrent prostate cancer: early results. *Scand J Urol Nephrol.* 2010;44:223–227.
20. Chalasani V, Martinez CH, Lim D, Chin J. Salvage HIFU for recurrent prostate cancer after radiotherapy. *Prostate Cancer and Prostatic Dis.* 2009;12:124–129.
21. Murota-Kawano A, Nakano M, Hongo S, Shoji S, Nagata Y, Uchida T. Salvage high-intensity focused ultrasound for biopsy-confirmed local recurrence of prostate cancer after radical prostatectomy. *BJU Int.* 2010;105:1642–1645.
22. Sanderson KM, Pensson DF, Cai J, et al. Salvage radical prostatectomy: quality of life outcomes and long-term oncological control of radiorecurrent prostate cancer. *J Urol.* 2006;176:2025–2032.
23. Crouzet S, Murat F-J, Pommier P, et al. Locally recurrent prostate cancer after initial radiation therapy: early salvage high-intensity focused ultrasound improves oncologic outcomes. *Radiother Oncol.* 2012;105:198–202.
24. Chapelon J-Y, Rouvière O, Crouzet S, Gelet A. Prostate focused ultrasound therapy. In: Escoffre J-M, Bouakaz A, eds. *Therapeutic Ultrasound.* Switzerland: Springer International Publishing; 2016:21–41.
25. Ahmed HU, Zacharakis E, Dudderidge T, et al. High-intensity-focused ultrasound in the treatment of primary prostate cancer: the first UK series. *Br J Cancer.* 2009;101:19–26.
26. Crouzet S, Chapelon JY, Rouvière O, et al. Whole-gland ablation of localized prostate cancer with high-intensity focused ultrasound: oncologic outcomes and morbidity in 1002 patients. *Eur Urol.* 2014;65:907–914.
27. Song W, Jung US, Suh YS, et al. High-intensity focused ultrasound as salvage therapy for patients with recurrent prostate cancer after radiotherapy. *Korean J Urol.* 2014;55:91.
28. Uchida T, Shoji S, Nakano M, et al. High-intensity focused ultrasound as salvage therapy for patients with recurrent prostate cancer after external beam radiation, brachytherapy or proton therapy. *BJU Int.* 2011;107:378–382.
29. Zacharakis E, Ahmed HU, Ishaq A, et al. The feasibility and safety of high-intensity focused ultrasound as salvage therapy for recurrent prostate cancer following external beam radiotherapy. *BJU Int.* 2008;102:786–792.
30. Fuller CD, Scarbrough TJ. Fiducial markers in image-guided radiotherapy of the prostate. *Oncol Hematol Rev (US).* 2006;00:75.
31. Kupelian PA, Langen KM, Willoughby TR, Zeidan OA, Meeks SL. Image-guided radiotherapy for localized prostate cancer: treating a moving target. *Semin Radiat Oncol.* 2008;18:58–66.
32. Seip R, Shaeffer D, Lawrence P, et al. Feasibility study for the treatment of brachytherapy failure prostate cancer using high-intensity focused ultrasound. In: *Third International Symposium on Therapeutic Ultrasound;* 2003.
33. Chapman AT, Rivens IH, Thompson AC, ter Haar GR. High intensity focused ultrasound (HIFU) as a salvage treatment for recurrent prostate cancer after brachytherapy - a feasibility study. In: *AIP Conference Proceedings.* Vol. 911. Melville, NY: AIP; 2007:405–410.
34. Chan MF, Cohen GN, Deasy JO. Qualitative evaluation of fiducial markers for radiotherapy imaging. *Technol Cancer Res Treat.* 2015;14:298–304.
35. Habermehl D, Henkner K, Ecker S, Jakel O, Debus J, Combs SE. Evaluation of different fiducial markers for image-guided radiotherapy and particle therapy. *J Radiat Res.* 2013;54:i61–i68.
36. Hellinger JC, Blacksberg S, Haas J, Melnick J. Interventional uroradiology in the management of prostate cancer. *Appl Radiol.* 2015;44:40–41.
37. Rudat V, Nour A, Hammoud M, Alaradi A, Mohammed A. Image-guided intensity-modulated radiotherapy of prostate cancer. *Strahlentherapie und Onkologie.* 2016;192:109–117.
38. Ye JC, Qureshi MM, Clancy P, Dise LN, Willins J, Hirsch AE. Daily patient setup error in prostate image guided radiation therapy with fiducial-based kilovoltage onboard imaging and conebeam computed tomography. *Quant Imaging Med Surg.* 2015;5:665–672.
39. van der Heide UA, Kotte AN, Dehnad H, Hofman P, Lagenijk JJ, van Vulpen M. Analysis of fiducial marker-based position verification in the external beam radiotherapy of patients with prostate cancer. *Radiother Oncol.* 2007;82:38–45.
40. Kotte AN, Hofman P, Lagendijk JJ, van Vulpen M, van der Heide UA. Intrafraction motion of the prostate during external-beam radiation therapy: analysis of 427 patients with implanted fiducial markers. *Int J Radiat Oncol Biol Phys.* 2007;69:419–425.
41. Ng M, Brown E, Williams A, Chao M, Lawrentschuk N, Chee R. Fiducial markers and spacers in prostate radiotherapy: current applications. *BJU Int.* 2014;113:13–20.
42. Shirato H, Harada T, Harabayashi T, et al. Feasibility of insertion/implantation of 2.0-mm-diameter gold internal fiducial markers for precise setup and real-time tumor tracking in radiotherapy. *Int J Radiat Oncol Biol Phys.* 2003;56:240–247.
43. Graf R, Wust P, Budach V, Boehmer D. Potentials of on-line repositioning based on implanted fiducial markers and electronic portal imaging in prostate cancer radiotherapy. *Radiat Oncol.* 2009;4:13.
44. Treeby BE, Cox BT. k-Wave: MATLAB toolbox for the simulation and reconstruction of photoacoustic wave fields. *J Biomed Opt.* 2010;15:021314.
45. Treeby BE, Jaros J, Rendell AP, Cox BT. Modeling nonlinear ultrasound propagation in heterogeneous media with power law absorption using a k-space pseudospectral method. *J Acoust Soc Am.* 2012;131:4324.
46. Chin JL, Billia M, Relle J, et al. Magnetic resonance imaging guided transurethral ultrasound ablation of prostate tissue in patients with localized prostate cancer: a prospective phase 1 clinical trial. *Eur Urol.* 2016;70:447–455.
47. Yutkin V, Ahmed HU, Donaldson I, et al. Salvage high-intensity focused ultrasound for patients with recurrent prostate cancer after brachytherapy. *Urol.* 2014;84:1157–1162.
48. Illing R, Emberton M. Sonablate 500: transrectal high-intensity focused ultrasound for the treatment of prostate cancer. *Expert Rev Med Devices.* 2006;3:717–729.
49. Uchida T, Nakano M, Shoji S, Nagata Y, Usui Y, Terachi T. Twelve years experience with high-intensity focused ultrasound (HIFU) using sonablate devices for the treatment of localized prostate cancer. In: *11th International Symposium on Therapeutic Ultrasound,* Vol. 1481, Melville, NY: AIP Conference Proceedings; 2012: 401–406.

50. Uchida T, Ohkusa H, Nagata Y, Hyodo T, Satoh T, Irie A. Treatment of localized prostate cancer using high-intensity focused ultrasound. *BJU Int.* 2006;97:56–61.
51. Berenger J-P. Three-dimensional perfectly matched layer for the absorption of electromagnetic waves. *J Comput Phys.* 1996;127:363–379.
52. Jaros J, Rendell AP, Treeby BE. Full-wave nonlinear ultrasound simulation on distributed clusters with applications in high-intensity focused ultrasound. *Int J High Perform Comput Appl.* 2016;30:137–155.
53. Jaros J, Nikl V, Treeby BE. Large-scale ultrasound simulations using the hybrid openMP/MPI decomposition. Exascale Applications and Software Conference; 2015.
54. Jalloh M, Leapman MS, Cowan JE, et al. Patterns of local failure following radiation therapy for prostate cancer. *J Urol.* 2015;194:977–982.